# Wall-modeled LES of laser-scanned rime, glaze, and horn ice shapes

**By B. Bornhoft, S. S. Jain, K. Goc, S. T. Bose† AND P. Moin**

## 1. Motivation and objectives

Predicting the aerodynamic performance of an aircraft in icing conditions is critical, as failures in an aircraft's ice protection system can compromise flight safety. Historically, studying aerodynamic effects of icing has typically relied on RANS modeling, which usually struggles to accurately predict the stall behavior, particularly in conditions in which the effect of ice accretion, at early times (less than one minute of accretion), is to only introduce surface roughness to an otherwise smooth surface (Rumsey *et al.* 2019).

In response to a series of icing-related accidents, the Federal Aviation Administration (FAA) implemented a new ruling in 2007 that modified the regulations that govern today's aircraft, which are found in Title 14 Code of Federal Regulations (CFR) Part 25 for Airworthiness Standards: Transport Category Airplanes, by adding a requirement to certify that transport-category airplanes exhibit the same handling/performance in both icing and non-icing conditions (FAA 2007). A follow-on change to both Parts 25 and 33, adding Appendix O, came into effect in 2015 and focused on extending the new certification requirement to both airframes and engines operating in supercooled large droplet (SLD) and ice crystal icing conditions (FAA 2014). These rule changes were largely in response to the 1994 accident in Roselawn, Indiana, where an Avions de Transport Régional (ATR) 72 series airplane experienced an un-commanded roll. The National Transportation Safety Board (NTSB) determined that the accident was caused due by freezing raindrops that created a spanwise ridge of ice downstream of the wing's deicing boot.

Prior to the addition of Appendix O, no certification was required for aircraft performance during freezing rain or drizzle events, which induce both SLD and ice crystals. The rule changes have drastically altered how aircraft manufacturers design their airplanes by requiring them to consider the effects of icing in the earliest stages of design. Early designs do not often include ice tunnel testing, primarily due to the cost associated with these tests. Therefore, aircraft designs under these rules rely heavily upon computational fluid dynamics (CFD) simulations. Hence there is a clear need to accurately predict and model ice accretion and its effect on aerodynamics.

The two primary types of icing are rime and glaze (Gent *et al.* 2000; Politovich 2019). Rime ice typically occurs at low flight temperatures ($< -20°$C), low speeds, low atmospheric liquid water concentration (LWC), and small droplet sizes. Rapid and complete freezing of the droplets impacting the aerodynamic surfaces leads to opaque accretion of ice on the wing's leading edge, which is still streamlined. Rime ice's primary aerodynamic impact comes from its characteristic roughness. Glaze ice occurs at higher flight temperatures (near freezing), higher speeds, high atmospheric LWC, and large droplet sizes. Upon impact, the droplets still attach to nucleation points on the wing, but due

† Cascade Technologies, Inc.

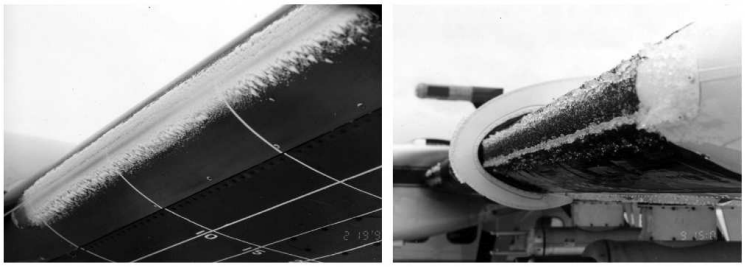

(a) (b)

FIGURE 1. Icing examples from a post-flight test by the NASA Glenn Research Center's instrumented Twin Otter aircraft: (a) rime ice conditions and (b) glaze ice conditions (Politovich 2019).

to larger droplet sizes, water will run back along the wing body and experience delayed freezing. This results in a translucent and smoother ice covering over the surface of the aircraft; and when exposed to icing conditions for longer time, glaze ice leads to so-called horn ice conditions. Ice horns can drastically impact the aerodynamic performance of an aircraft by inducing separation at modest angles of attack, leading to an overall decrease in maximum lift and stall angle (Gent *et al.* 2000). Figure 1 shows examples of (a) rime and (b) glaze ice from a flight test.

Encouraged by recent studies using large-eddy simulations (LES) that demonstrate the ability to predict stall characteristics on full aircraft at affordable costs (Goc *et al.* 2021), we aim to apply this methodology to icing conditions. Measurements of lift, drag, and pitching moment of a NACA23012 airfoil under rime and glaze ice conditions are available at $Re = 1.8$ million (M) in the work of Broeren *et al.* (2018). Using laser scanned, detailed representations of the iced geometries from Broeren *et al.* (2018), we perform LES calculations to assess the aerodynamic impact of the ice in various conditions. The simulations are validated by comparing the integrated loads against experimental measurements in both clean and iced conditions at various angles of attack through the onset of stall.

Most previous studies that predict icing and its effect on aerodynamic performance use lower-fidelity modeling approaches, such as Reynolds-averaged Navier–Stokes (RANS) equations (Morency *et al.* 2001; Habashi *et al.* 2003; Aliaga *et al.* 2007; Chi *et al.* 2005; Hann *et al.* 2020). More recently, glaze and horn ice shapes have been simulated using detached-eddy simulation (DES) in Pan & Loth (2005), lattice-Boltzmann methods (LBM) in König *et al.* (2015), zonal LES in Duclercq *et al.* (2012), dynamic hybrid RANS/LES in Alam *et al.* (2015), and wall-modeled LES (WMLES) in Xiao *et al.* (2020). These more recent studies showed improved results over those using RANS methods, but focused only on ice shapes with relatively large obstructions. To the authors' knowledge, higher-fidelity approaches have not been applied to rime ice shapes with less than one minute of ice accretion, herein referred to as early-time ice accretion.

In this work, we use WMLES to study the effects of both rime and glaze icing conditions on aerodynamic performance. Three ice shapes are considered: two early-time ice shapes (one each for rime and glaze ice conditions), with accretion times of less than one minute, and one long-time horn ice shape, after five minutes of glaze ice accretion. At first, ice introduces only roughness to the surface, but after long accretion, large deformations are eventually introduced to the otherwise clean surface. The viability of the WMLES as a

tool to predict the effect of icing on aircraft aerodynamics in these various conditions is assessed.

## 2. Effects of icing: experimental data

NASA Glenn's Icing Research Tunnel (IRT) has led research on the effect of ice accretion on aerodynamic bodies since 1944 (Potapczuk 2013). The IRT creates a cloud of supercooled water droplets from a series of spray bars that target various droplet diameter ranges, LWC, and temperatures. Recently, laser-scanning techniques have been developed and tested for iced airfoils in the IRT (Lee *et al.* 2014). This advancement provides digital representations of iced airfoils that can be used with rapid prototyping methods (RPM) for manufacturing ice shapes.

Glaze, rime, and horn ice geometries obtained using the laser scanner are shown along with the clean NACA23012 geometry in Figure 2. Here, $k/c$ describes the roughness length scale ($k$) normalized by the clean airfoil chord length ($c$). The value of $h$ is defined as the displacement height due to ice accretion with respect to a clean geometry. The value of $k$ is defined in this study as the root mean square of the displacement height minus its average across the surface, as seen in Eq. 2.1.

$$k \approx \sqrt{(h - \bar{h})^2} \tag{2.1}$$

The two length scales represent the bimodal behavior of ice accretion, whereby the ice geometrically modifies the airfoil outer mold line (represented by $h$) and also introduces additional roughness scales (represented by $k$). Figure 2 shows the (d) lift ($C_L$), quarter-chord pitching moment ($C_M$), and (e) wake drag ($C_D$) coefficients for the clean, glaze, rime, and horn ice geometries obtained from the experimental results of Broeren *et al.* (2018). Each geometry results in an early onset of stall accompanied by a significant rise in drag and an increased nose-down pitching moment. Similar to the clean airfoil, the rime ice geometry results in an aggressive stall behavior with a sharp decrease in $C_L$. By contrast, the glaze and horn ice geometries result in a shallower stall behavior with an earlier onset of stall. For the two early-time ice geometries, the scales of ice are less than 1% of the chord length yet still result in a drastic reduction in aerodynamic performance. The horn ice geometry yields the largest aerodynamic effect given its larger and irregular shape, with a region of a nose-up pitching moment at moderate angles of attack ($\alpha \approx 4 - 6^{\circ}$).

## 3. Modeling approach

We utilize LES techniques to simulate the various ice shapes. These methods rely on resolving the large scales and providing closure models for turbulence in the sub-grid regime. The solver employed is CharLES (Ham *et al.* 2004), a second-order low-dissipation finite-volume solver. We solve the governing equations for a low-pass filtered, compressible Navier–Stokes system for mass, momentum, and total energy. The numerical scheme has been shown to be suitable for coarsely resolved LES of turbulent flows that are especially sensitive to numerical dissipation. The discretization is suitable for arbitrary unstructured, polyhedral meshes, and the solutions contained herein are computed from unstructured grids based on Voronoi diagrams. The use of Voronoi diagram based meshes allows for the rapid generation of high-quality grids with some guaranteed properties (for instance, the vector between two adjacent Voronoi sites is parallel to the normal of the

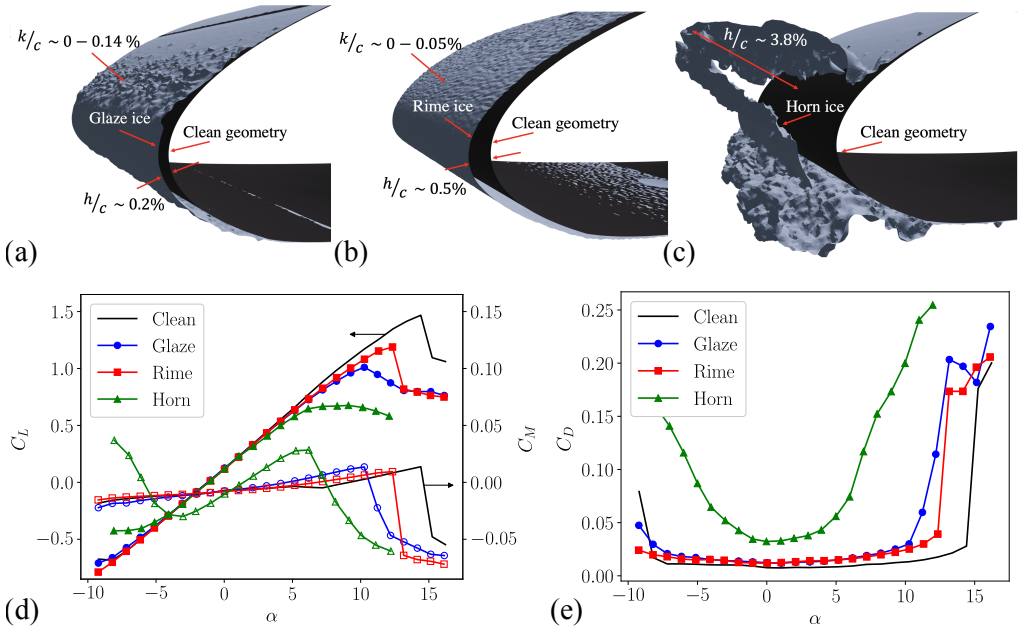


FIGURE 2. Top figures illustrate the geometric changes due to the (a) early-time glaze, (b) early-time rime, and (c) horn ice accretions on the NACA23012 clean geometry detailing ice scales that geometrically modify the airfoil outer mold line ($h$) and roughness scales ($k$). Bottom figures show the experimental (d) lift ($C_L$, closed symbols), quarter-chord pitching moment ($C_M$, open symbols), and (e) wake drag ($C_D$) coefficients for the clean, glaze, rime, and horn ice airfoils from Broeren *et al.* (2018).

face that they share). Time advancement is performed using a three-stage explicit Runge Kutta scheme (Gottlieb *et al.* 2001), and the spatial discretization is formally second-order accurate. Additional details of the numerical discretization and grid generation can be found in Fu *et al.* (2021), Lozano-Duran *et al.* (2020), and Bres *et al.* (2018). Sub-grid closures are modeled using the dynamic Smagorinsky approach of Germano *et al.* (1991). Near-wall regions are modeled using an equilibrium wall-modeling approach in which we assume the pressure gradient balances the advective terms leading to a constant stress layer (Bose & Park 2018). We then apply a stress at the wall based on an assumed log law in the boundary layer profile.

## 4. Computational setup

The cases simulated utilize the NACA23012 two-dimensional airfoil. The flow field is characterized by a free-stream Mach number ($M_\infty$) of 0.18 and a chord-based Reynolds number ($Re_c$) of 1.8 M. As noted above, four geometries are considered in this study. The first is a clean version of the NACA23012 geometry. The next two are early-time glaze and rime ice accretion geometries [designated ED1974 and ED1983 respectively in Broeren *et al.* (2018)]. The last is a longer-duration horn ice geometry [designated ED1978 in Broeren *et al.* (2018)]. Here, we refer to the cases as clean, glaze ice, rime ice, and horn ice. A set of angles of attack ($\alpha$) are simulated by rotating the airfoil about the quarter chord. As shown in Figure 3 (a), the geometries are modeled in a rectangular domain.

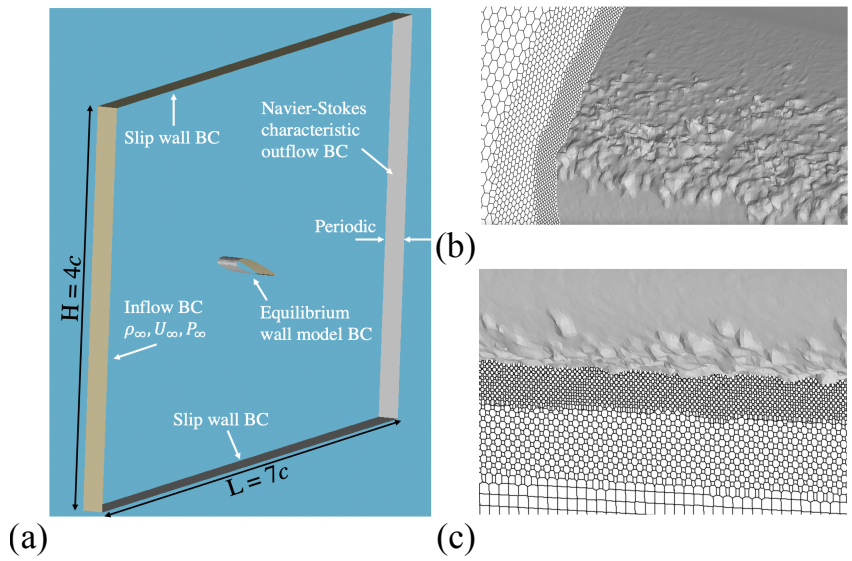


FIGURE 3. (a) Schematic showing the computational domain setup highlighting the inflow boundary condition (BC), outflow BC, equillibrium wall model BC (applied on the airfoil surface), slip wall BC for the top and bottom of the domain, and periodic BC in the spanwise direction. (b,c) HCP element slices highlighting the resolution near rough surfaces: (b) spanwise and (c) streamwise slices. Lengths are defined with respect to the chord length ($c$).

A span of $0.125c$ is used for the clean and rime ice geometries, $0.2c$ for the glaze ice geometry, and $0.25c$ for the horn ice geometry. Inflow conditions are specified using free-stream pressure, density, and Mach number ($P_\infty = 101,325$ Pa, $\rho_\infty = 1.225$ kg/m$^2$, and $M_\infty = 0.18$). The outflow boundary is represented by the non-reflecting characteristic boundary condition of Poinsot & Lele (1992). The top and bottom of the domain are modeled using inviscid boundary conditions. A viscous algebraic equilibrium wall model is applied at the airfoil surfaces (Lehmkuhl *et al.* 2016). The spanwise boundaries are treated as periodic conditions. Periodicity is forced on the horn ice case by mirroring a spanwise section of $0.125c$. Statistics are gathered throughout the simulation and averaged across at least 30 chord-based flow-through times.

In Figure 3, we show the water-tight geometries of the airfoils surrounded by a bounding surface box that is used as the surfaces for generating a Voronoi diagram following the algorithm proposed by Du *et al.* (2006). Figure 3 (b,c) illustrates the ability of the Voronoi points to resolve the complex roughness elements present in the ice. The coarsest grid for the clean ice geometry contains $\sim 1.2$ M control volumes (CV). Each successive grid is obtained by homothetically refining the cells by a factor of two. Each additional layer adds ten cells in the wall-normal direction and isotropically refines the elements in the other two directions. This results in $\sim 4$ Mcv for the medium clean case. Approximate grid cell counts, number of points per chord, and number of points per trailing edge boundary layer height ($\delta/\Delta_{min}$) are detailed in Table 1. Here, $\delta$ is the boundary layer thickness, and $\Delta_{min}$ is the minimum grid length scale in the mesh. An additional level of refinement is added for the first quarter of the chord, as it was observed that leading edge refinement contributed to capturing the correct separation behavior at higher angles of attack. Figure 4 plots the non-dimensional wall distance ($y^+$), normalized by the ratio of the friction velocity and the kinematic viscosity, projected on the airfoil surface from the

| Geometry | Refinement level | Cell count (M CV) | $\delta/\Delta_{min}$ | Cells/$c$ |
|---|---|---|---|---|
| Clean | Coarse | 1.2 | 8 | 780 |
| | Medium | 4 | 14 | 1,560 |
| | Fine | 14.25 | 25 | 3,125 |
| | Extra fine | 54 | 40 | 6,250 |
| Glaze | Coarse | 2 | 8 | 780 |
| | Medium | 7.15 | 14 | 1,560 |
| | Fine | 27 | 25 | 3,125 |
| Rime | Fine | 21 | 25 | 3,125 |
| | Extra fine | 109 | 40 | 6,945 |
| Horn | Fine | 34 | 25 | 3,125 |

TABLE 1. Grid refinement details for the different geometries comparing refinement levels; cell counts in millions of control volumes (M CV); points per boundary layer thickness ($\delta$), where $\Delta_{min}$ is the minimum grid length scale; and cells per chord length (c). Note: All values of $\delta/\Delta_{min}$ are referenced with respect to the clean ice simulation's boundary layer height at the trailing edge of the airfoil.

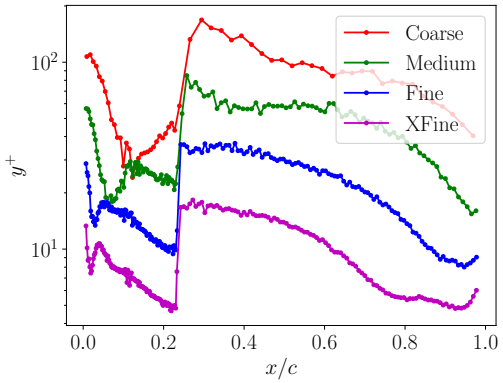


FIGURE 4. Conditionally averaged non-dimensional wall distance ($y^+$) along the streamwise coordinate projected on the airfoil surface from the first cell centroid along the suction side of the airfoil for the coarse, medium, fine, and extra fine (XFine) grid levels.

first cell centroid along the suction side of the airfoil. The average $y^+$ for the fine grid case is $\sim 13$ in the leading edge area and $\sim 28$ across the rest of the chord.

## 5. Results

### 5.1. *NACA23012 clean airfoil*

Accurate prediction of lift, drag, and moment coefficients for the clean airfoil geometry are necessary to establish simulation credibility before simulating the airfoil using various ice geometries. In Figure 5, aerodynamic coefficients are plotted as a function of

the angle of attack for a series of grid resolutions. We compare the experimental data of Broeren *et al.* (2018) in each case. We compare the uncorrected force balance measurements based on domain size sensitivity simulations. From these simulations, it was observed that the chosen domain is more representative of the wall-bounded wind tunnel rather than a free-air configuration. In addition to force balance measurements, a wake rake determines momentum losses across the airfoils. We include these measurements in the drag coefficient comparisons of Figure 5(b) (Monastero 2014). König *et al.* (2015) previously used an LBM to simulate the clean, glaze ice, and horn ice geometries present in the current study. No other references yet exist for simulating these ice geometries other than our simulations and the LBM results.

As the angle of attack increases, the lift coefficient linearly increases while the moment and drag coefficients remain relatively consistent, with minor increases nearing the critical stall angle. Around $\alpha = 14^{\circ}$, a sharp decline in lift occurs due to the rapid onset of stall. This is accompanied by a nose-down pitching moment and a rapid rise in drag. We note that the LBM results do not show the stall that is seen in the experiments of Broeren *et al.* (2018). König *et al.* (2015) attribute this to not correctly reproducing a laminar separation bubble at the leading edge of the airfoil. While the WMLES solution also does not resolve a laminar separation bubble, the results presented here show stall behavior starting with the medium grid resolution. Upon further refinement, the stall is more representative of the experimental data, albeit not as abrupt. In the linear region of the lift curve, both methods overpredict the slope of the lift curve. An extra fine resolution is simulated at higher angles of attack. Here, the additional refinement leads to an excellent agreement in the linear regime just prior to stall. One additional simulation with no-slip wall boundaries was run and yielded different results for the integrated quantities. This result ensures that the simulations are still within the limit of wall modeling. A general improvement is observed compared to the previous LBM results across all quantities. The overprediction of a nose-down pitching moment at finer angles of attack is discussed in Section 5.2.1, relating the phenomenon to spanwise periodic restrictions. For this study, the results of the clean airfoil are acceptable, as they have improved upon previous results in the literature and capture the experimental stall behavior. We report the fine grid results when comparing them to other ice cases. We choose this resolution because it is considered tractable for simulating more complicated configurations of interest, such as swept wings, engine nacelles, and the high-lift common research model, under icing conditions (Goc *et al.* 2021).

### 5.2. *Glaze ice geometry*

The first ice geometry we simulate is an early-time glaze ice case, as shown in Figure 2(a). The glaze ice geometry has a smooth ice section near the leading edge, with roughness elements downstream on both the upper and lower wing surfaces. Prolonged exposure to icing conditions for this geometry leads to ice horns. As stated in Section 5.1, we use the fine grid resolution as our benchmark. Table 1 has a total grid count of 27 M CV for the glaze ice case. The increase in total control volumes is due to the finest resolution being applied to any region that includes ice and a change in the spanwise extent up to $0.2c$. Similar to the clean ice case, we compare the uncorrected experimental results and the results of König *et al.* (2015) in Figure 6. Improved results are observed compared to those of König *et al.* (2015) for the lift and drag coefficients in the present study. Here, the stall is less pronounced than that of the clean airfoil. The roughness elements immediately trigger the boundary layer transition. This roughness-triggered transition can be observed in the comparison of velocity magnitude slices with wall-shear-stress colored surfaces in

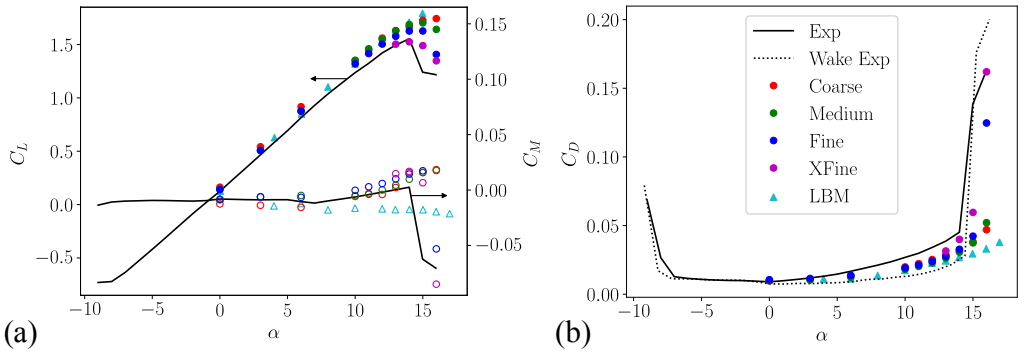


FIGURE 5. Comparing (a) lift ($C_L$, closed symbols), moment ($C_M$, open symbols), (b) and drag ($C_D$) coefficients of the present WMLES results at four grid resolutions to experimental wake (·····) and force balance (——) measurements (Broeren *et al.* 2018) as well as LBM results (König *et al.* 2015) for the clean NACA23012 geometry as a function of angle of attack ($\alpha$). The legend applies to both panels.

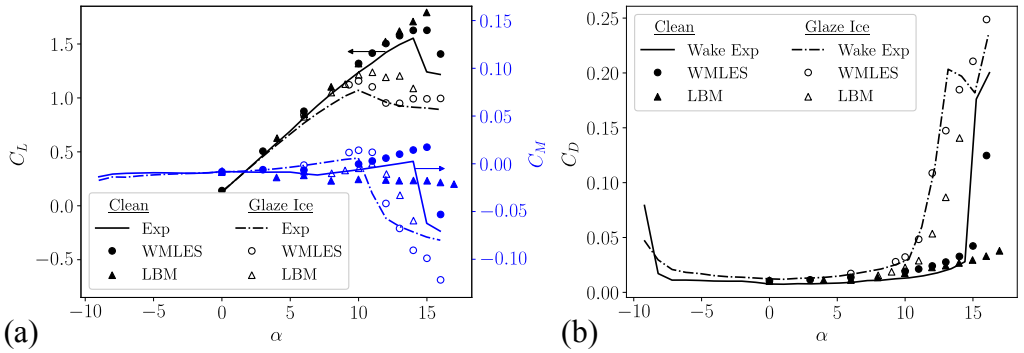


FIGURE 6. (a) Lift ($C_L$), moment ($C_M$), and (b) drag ($C_D$) coefficients comparing the clean (closed symbols, ——) and glaze ice (open symbols, -·-·) geometries of the experimental (Broeren *et al.* 2018), LBM (König *et al.* 2015), and present WMLES results.

Figure 7. The WMLES results predict the stall angle of attack correctly, while the LBM method predicts stall at one degree past the experimental measurement. The stall is less abrupt, with a shallower post-stall $C_L$ slope. The lift coefficient levels off in the post-stall region, which is observed in the WMLES results as well. In Figure 6(b), drag coefficients between the methods are compared. At stall, both the clean and glaze ice geometries undergo a rapid rise in drag due to the onset of separation. A non-monotonic behavior in drag is observed in the experimental wake drag results. This non-monotonicity was not present in the force balance measurements. Generally, we find good agreement between our WMLES calculations and the experimental results.

The moment coefficients are drastically underpredicted in the post-stall region as compared to both the experimental and LBM results. Section 5.2.1 discusses why the moment coefficients are predicted to be largely negative, unlike to the experimental data.

### 5.2.1. *Spanwise variation*

Highly negative moments in the stalled region of the glaze ice case where the lift coefficients are reasonable compared to the experimental data suggest an issue of domain constriction. Indeed, if we look at a snapshot of the resulting flow field (see Figure 8),

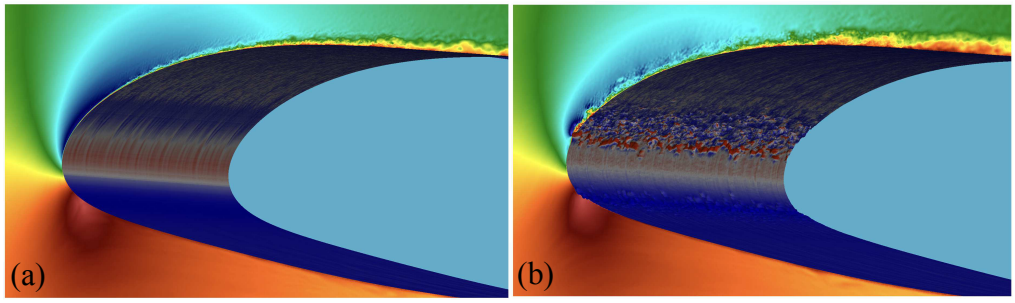


FIGURE 7. Center-line flow-field slice colored by velocity magnitudes with surface plot colored by wall shear stress of (a) NACA23012 clean geometry and (b) early glaze ice geometry, both at $\alpha = 9.3^{\circ}$.

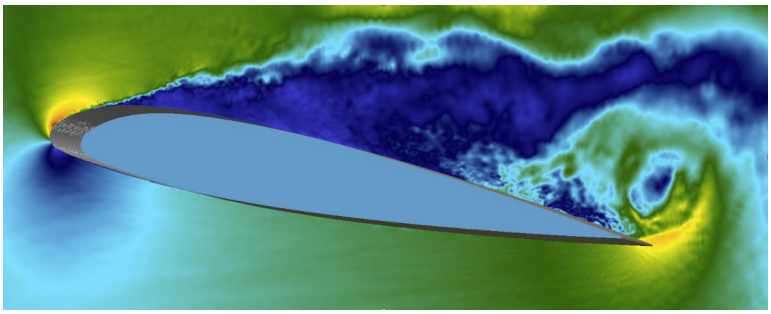

FIGURE 8. Instantaneous center-line flow-field snapshot of velocity magnitude during a sixteen degree angle of attack ($\alpha = 16^{\circ}$) simulation.

we observe two-dimensional vortical structures. These are believed to be caused by the spanwise restriction imposed by using a periodic domain with a $0.2c$ extent. To investigate this further, we conduct an increasing spanwise study at $\alpha = 9.3^{\circ}, 14^{\circ}$, and $16^{\circ}$. Table 2 shows the details of the grids for the new spanwise study. Each successive case doubles the span of the simulation. In Figure 9, spanwise conditioned pressure coefficients are plotted as a function of $x/c$, where $x$ is the spatial location along the chord. Minimal changes are observed near the leading edge ($x/c < 0.2$).

Around $x/c = 0.85$, a small pocket of lower $C_p$ is observed. This region is indicative of a region of lift that is far from the center of the quarter-chord moment. As the span is increased, this pocket minimizes, indicating that it is an artifact of the spanwise restricted flow field at high angles of attack. Indeed, in Figure 10(a), we observe drastic changes in the moment coefficients for high angles of attack. Increasing the span reduces the magnitude of the nose-down pitching moment and brings it into agreement with the experimental results. In contrast, as the span is increased, minimal changes are observed in the lift coefficients [Figure 10(a)]. Figure 10(b) compares the drag coefficient for each span. At $\alpha = 9.3^{\circ}$, minor sensitivity to the spanwise extent is observed. At higher angles of attack, the drag decreases. When simulating post-stall angles of attack, it is necessary to select a spanwise extent that minimizes errors due to the two-dimensional flow restrictions. This is especially necessary for predicting the moment coefficients.

| Geometry | Span | Cell count (M CV) |
|---|---|---|
| Glaze | $0.2c$ | 27 |
| | $0.4c$ | 43 |
| | $0.8c$ | 85 |
| | $1.6c$ | 170 |

TABLE 2. Details of the spanwise extent study detailing the span with respect to the chord length and cell count for each simulation.

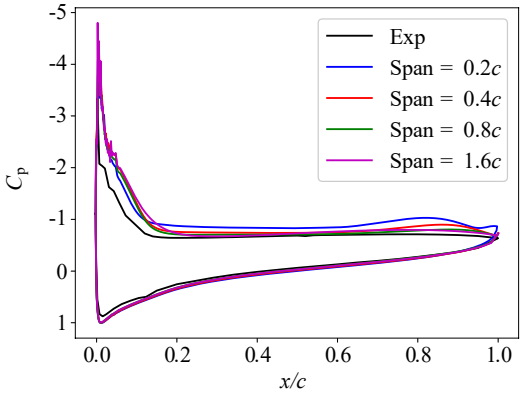


FIGURE 9. Sensitivity of pressure coefficients ($C_P$) as a function of $x/c$ with increasing span with comparisons to experimental pressure measurements (Broeren *et al.* 2018).

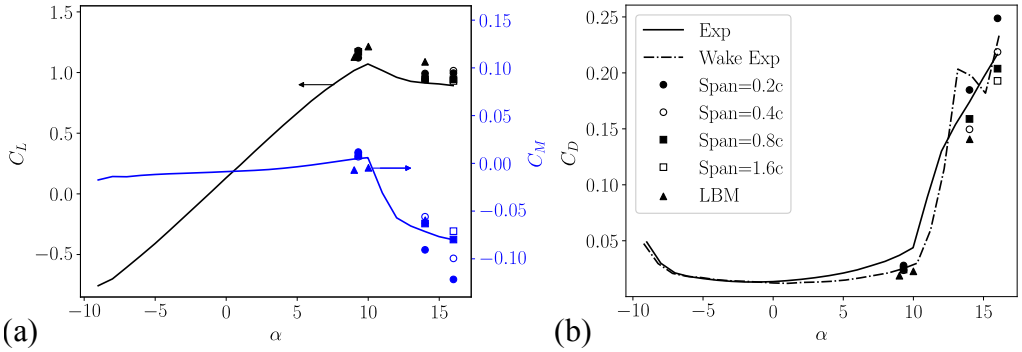


FIGURE 10. Sensitivity of (a) lift ($C_L$), moment ($C_M$), and (b) drag ($C_D$) coefficients for the glaze ice geometry with increasing span with comparisons to experimental wake (-·-·-) and force balance (——) measurements (Broeren *et al.* 2018) as well as LBM simulations (König *et al.* 2015). The legend applies to both panels.

### 5.3. *Rime ice geometry*

The second geometry we simulated is the early-time rime ice case, as shown in Figure 2(b). The rime ice case was formed in cold conditions ($-22^{\circ}$C). Unlike the glaze ice case, the roughness is distributed evenly across the upper and lower surface of the NACA23012

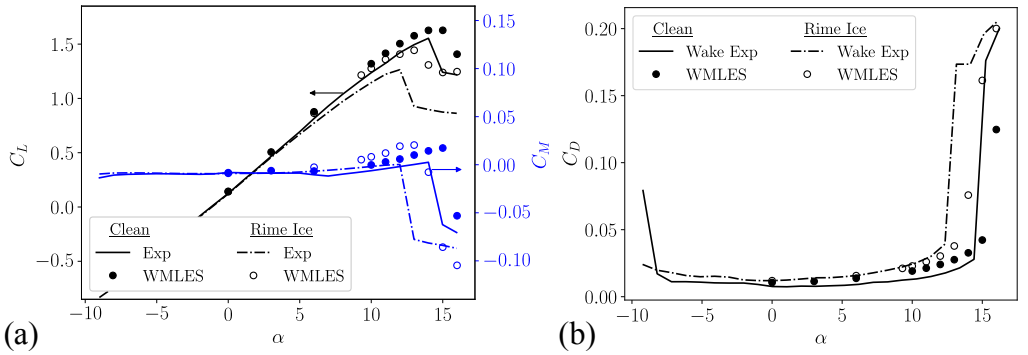


FIGURE 11. (a) Lift ($C_L$), moment ($C_M$), and (b) drag ($C_D$) coefficients comparing the clean (closed symbols, ——) and rime ice (open symbols, -·-·) geometries of the experimental (Broeren *et al.* 2018) and present WMLES results.

airfoil. We apply the established practices from the glaze ice simulations to the rime ice geometry. To the authors' knowledge, these are the first-ever simulations of a laser-scanned rime ice geometry.

In Figure 11, lift, drag, and moment coefficients are compared to the experimental data. Contrary to the glaze ice case, the rime ice case does not predict the correct change in lift and drag. The maximum lift and critical stall angle are both overpredicted. The delayed separation can also be observed when comparing the wake drag measurements to the simulated results. These mispredictions are due to the under-resolved roughness scales near the leading edge. The maximum roughness height,as a percentage of chord length ($k_{max}/c$) is approximately 0.03% for the rime ice geometry. This results in about 1.5 control volumes per maximum roughness height. This means all of the roughness scales are in the sub-grid scale regime.

In Figure 12, we take three angles of attack and refine the grid to an additional level (equivalent to the extra fine clean airfoil simulation). It can be observed that predictions of the lift, drag, and moment coefficients improve with respect to the experimental data. There are approximately 3 control volumes per maximum roughness height at this resolution. For the methods used in this work, the recommended number of points per roughness height is 3-6. Here, we are beginning to resolve the roughness scales, but further refinement is required to resolve all of the scales appropriately. In Figure 13, we compare the qualitative features of the flow field. Figure 13(a) corresponds to the fine case, while Figure 13(b) corresponds to the extra fine case. Comparing the two results highlights that the roughness elements are completely sub-grid for the fine grid simulations. We observe streaks in the wall shear stress that are qualitatively similar to those seen with the clean geometry. The near-wall streaks are destroyed for the extra fine case due to the roughness elements. Regions of increased wall shear stress can be observed in the regions with rime ice roughness. The additional refinement required to capture the roughness elements appropriately becomes intractable when simulating a wing or complete aircraft under similar resolutions. Therefore, these results highlight the need for roughness wall models in rime ice conditions.

### 5.4. *Horn ice geometry*

Lastly, we assess the LES approaches for the horn ice geometry, as shown in Figure 2(c). In Figure 14, the lift, moment, and drag coefficients from the simulated results are compared

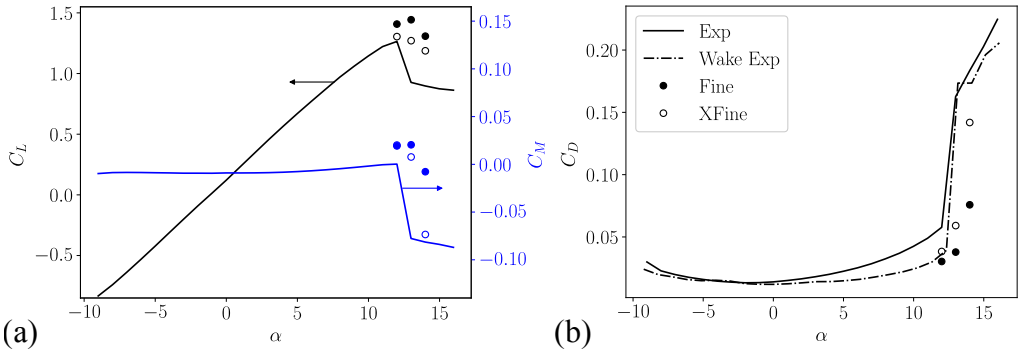


FIGURE 12. Sensitivity of (a) lift ($C_L$), moment ($C_M$), and (b) drag ($C_D$) coefficients for the rime ice geometry with increasing grid resolution with comparisons to experimental wake (-·-·-) and force balance (——) measurements (Broeren *et al.* 2018). The legend applies to both panels.

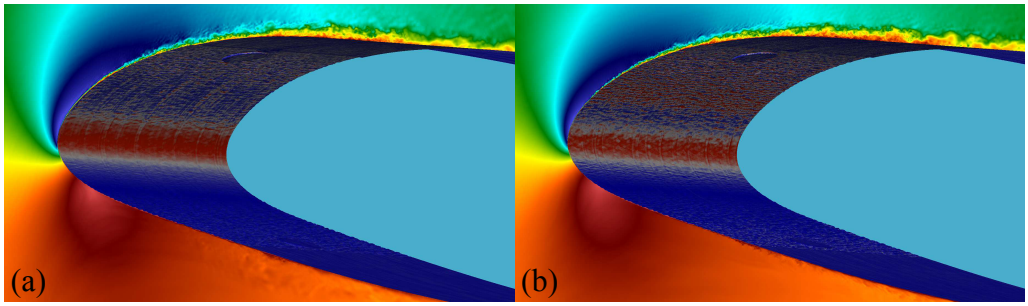


FIGURE 13. Center-line flow-field slice colored by velocity magnitudes with surface plot colored by wall shear stress of (a) fine and (b) extra-fine rime ice geometry at $\alpha = 12^{\circ}$.

to the experimental and LBM results. We observe good agreement with the experimental data for the horn ice case. Similar results are obtained for the LBM approach. At high angles of attack, we observe overpredicted drag and underpredicted moments. Future studies will focus on grid refinement and spanwise variation for the horn ice geometry. The horn ice case is, in some ways, less challenging for WMLES simulations, but more challenging for constructing body-fitted meshes due to the complex geometric features. In Figure 15, an instantaneous center-line slice colored by the velocity magnitudes shows how the flow is immediately separated downstream of the horn ice shape even for a moderate angle of attack ($\alpha = 5^{\circ}$). Wall shear stress contours on the surface highlight the localized value of shear at the tips of the ice horns. Flow separation occurs due to the geometric obstruction of the horns, whereas the other geometries, with more minor ice accretion levels, have less intrusive separation mechanisms.

## 6. Conclusions

Three NACA23012 ice geometries have been simulated using WMLES. These included rime, glaze, and horn ice cases. Additional simulations of the clean NACA23012 geometry built credibility for our modeling approaches. Comparisons to the experimental work of Broeren *et al.* (2018) and the numerical result of König *et al.* (2015) for lift, drag, and moment coefficients were made for each of the geometries. In this work, we observe both qualitative and quantitative agreement with the experimental data and better agree-

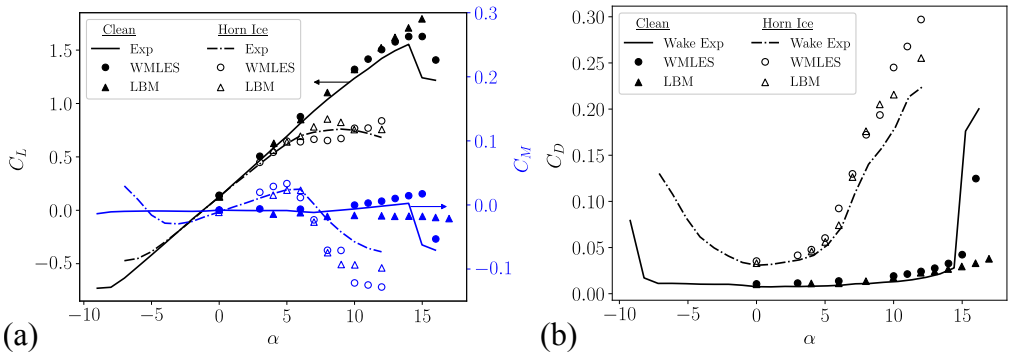


FIGURE 14. (a) Lift ($C_L$), moment ($C_M$), and (b) drag ($C_D$) coefficients comparing the clean (closed symbols, ——) and horn ice (open symbols, -·-·-) geometries of the experimental (Broeren *et al.* 2018), LBM (König *et al.* 2015), and present WMLES results.

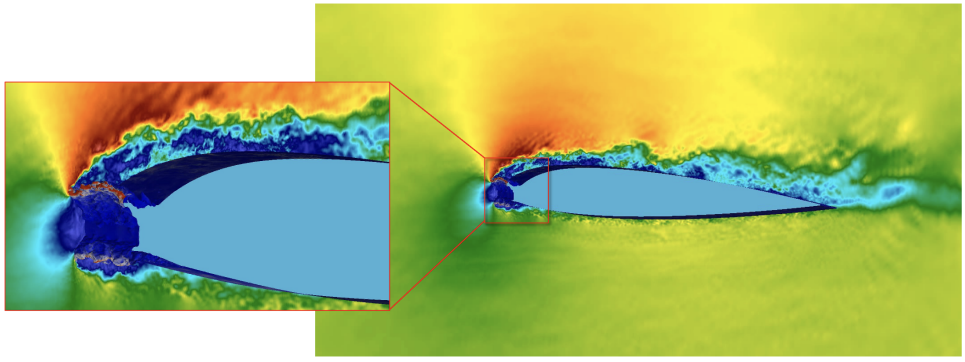

FIGURE 15. Center-line flow-field slice colored by velocity magnitudes with surface plot colored by wall shear stress of the NACA23012 airfoil at $\alpha = 5^\circ$ with horn ice. Inset focuses on the leading edge of the airfoil, highlighting the high shear stress near the ends of each horn.

ment compared to the previous numerical results. This is due to the combination of our modeling choices: Voronoi grid generation that can resolve complex roughness elements, low-dissipation numerics, advanced wall modeling, and dynamic sub-grid models. Sensitivities to grid resolution and spanwise extent were explored. Geometries with larger ice shapes relative to the airfoil chord required lower grid resolution. Shapes with small-scale roughness, such as the rime ice shape, required additional refinement to resolve the roughness scales. These resolution requirements are deemed too restrictive for general application; therefore, we conclude that rime ice geometries would benefit from specific roughness wall modeling. It was observed that increasing the spanwise extent was necessary to capture the airfoil moments in the post-stall regime adequately. These efforts build confidence in using WMLES for complex ice shapes. Future work will include additional ice shapes to build simulation credibility for all ice shapes that can be observed in flight.

## Acknowledgments

This investigation was funded by the Boeing Co. and the DoD SMART Fellowship. We acknowledge the generous computing resources for the DOE's ALCC and PSAAP III

programs. The authors would like to thank Dr. Andy Broeren and Dr. Sam Lee of NASA Glenn Research Center for the valuable discussions and for providing the laser-scanned geometries that were used in the simulations.

## REFERENCES

Alam, M. F., Thompson, D. S. & Walters, D. K. 2015 Hybrid Reynolds-averaged Navier-Stokes/large-eddy simulation models for flow around an iced wing. *J. Aircr.* **52**, 244–256.

Aliaga, C. N., Aubé, M. S., Baruzzi, G. S., Habashi, W. G. & Nadarajah, S. 2007 A third-generation in-flight icing code: FENSAP-Ice-Unsteady. *SAE Trans.* 116, 697–703.

Bose, S. & Park, G. 2018 Wall-modeled large-eddy simulation for complex turbulent flows. *Annu. Rev. Fluid Mech.* **50**, 535–561.

Bres, G., Bose, S., Emory, M., Ham, F., Schmidt, O., Rigas, G. & Colunius, T. 2018 Large-eddy simulations of co-annular turbulent jet using a voronoi-based mesh generation framework. *AIAA Paper* 2018–3302.

Broeren, A. P., Addy, Jr, H. E., Lee, S., Monastero, M. C. & McClain, S. T. 2018 Three-dimensional ice-accretion measurement methodology for experimental aerodynamic simulation. *J. Aircr.* **55**, 817–828.

Chi, X., Li, Y., Addy, H., Addy, G., Choo, Y., Shih, T. & Chen, H. 2005 A comparative study using CFD to predict iced airfoil aerodynamics. *AIAA Paper* 2005–1371.

Du, Q., Emelianenko, M. & Ju, L. 2006 Convergence of the Lloyd algorithm for computing centroidal Voronoi tessellations. *SIAM J. Numer. Anal.* **44**, 102–119.

Duclercq, M., Brunet, V. & Moens, F. 2012 Physical analysis of the separated flow around an iced airfoil based on ZDES simulations. *AIAA Paper* 2012–2798.

Federal Aviation Administration (FAA), DOT. 2007 Airplane performance and handling qualities in icing conditions. Final rule. *Federal register* **72**, p. 44656.

Federal Aviation Administration (FAA), DOT. 2014 Airplane and engine certification requirements in supercooled large drop, mixed phase, and ice crystal icing conditions. Final rule. *Federal register* **79**, p. 65508.

Fu, L., Karp, M., Bose, S., Moin, P. & Urzay, J. 2021 Shock-induced heating and transition to turbulence in a hypersonic boundary layer. *J. Fluid Mech.* **909**, A8.

Gent, R. W., Dart, N. P. & Cansdale, J. T. 2000 Aircraft icing. *Phil. Trans. R. Soc. A* **358**, 2873–2911.

Germano, M., Piomelli, U., Moin, P. & Cabot, W. H. 1991 A dynamic subgrid-scale eddy viscosity model. *Phys. Fluids* **3**, 1760–1765.

Goc, K. A., Lehmkuhl, O., Park, G. I., Bose, S. T. & Moin, P. 2021 Large eddy simulation of aircraft at affordable cost: a milestone in computational fluid dynamics. *Flow* **1**, E14.

Gottlieb, S., Shu, C.-W. & Tadmor, E. 2001 Strong stability-preserving high-order time discretization methods. *SIAM Rev.* **43**, 89–112.

Habashi, W. G., Morency, F. & Beaugendre, H. 2003 FENSAP-ICE: A second generation 3D CFD-based in-flight icing simulation system. *SAE Tech. Paper* 2003-01-2157.

Ham, F., Mattsson, K. & Iaccarino, G. 2004 Accurate and stable finite volume op-

erators for unstructured flow solvers *Annual Research Briefs*, Center for Turbulence Research, Stanford University, pp. 243–261.

Hann, R., Hearst, R. J., Sætran, L. R. & Bracchi, T. 2020 Experimental and numerical icing penalties of an S826 airfoil at low Reynolds numbers. *Aerospace* **7**, 46.

König, B., Fares, E. & Broeren, A. P. 2015 Lattice-Boltzmann analysis of three-dimensional ice shapes on a NACA 23012 airfoil. *SAE Tech. Paper* 2015-01-2084.

Lee, S., Broeren, A. P., Kreeger, R. E., Potapczuk, M. & Utt, L. 2014 Implementation and validation of 3D ice accretion measurement methodology. *AIAA Paper* 2014–2613.

Lehmkuhl, O., Park, G. & Moin, P. 2016 LES of flow over the NASA common research model with near-wall modeling. *Proceedings of the Summer Program*, Center for Turbulence Research, Stanford University, pp. 335–341.

Lozano-Duran, A., Bose, S. T. & Moin, P. 2020 Prediction of trailing edge separation on the NASA juncture flow using wall-modeled LES. *AIAA Paper* 2020-1776.

Monastero, M. 2014 Validation of 3D ice accretion documentation and replication method including pressure-sensitive paint. Master's thesis (unpublished), *University of Illinois at Urbana-Champaign*.

Morency, F., Beaugendre, H., Baruzzi, G. & Habashi, W. 2001 FENSAP-ICE—a comprehensive 3D simulation system for in-flight icing. *AIAA Paper* 2001–2566.

Pan, J. & Loth, E. 2005 Detached eddy simulations for iced airfoils. *J. Aircr.* **42**, 1452–1461.

Poinsot, T. & Lele, S. 1992 Boundary conditions for direct simulations of compressible viscous flows. *J. Comput. Phys.* **101**, 104–129.

Politovich, M. 2019 Aircraft icing. *Encyclopedia of Atmospheric Sciences*, J. R. Holton, Ed., Academic Press, 68–75.

Potapczuk, M. G. 2013 Aircraft icing research at NASA Glenn Research Center. *J. Aero. Eng.* **26**, 260–276.

Rumsey, C. L., Slotnick, J. P. & Sclafani, A. J. 2019 Overview and summary of the Third AIAA High Lift Prediction Workshop. *J. Aircr.* **56**, 621–644.

Xiao, M., Zhang, Y. & Zhou, F. 2020 Numerical investigation of the unsteady flow past an iced multi-element airfoil. *AIAA J.* **58**, 3848–3862.